Supplemental material for: "Pressure tuning of intrinsic and extrinsic sources to the anomalous Hall effect in $CrGeTe_3$"

Gili Scharf,[1] Daniel Guterding,[2] Bar Hen,[1] Paul M. Sarte,[3] Brenden R. Ortiz,[3] Gregory Kh. Rozenberg,[1] Tobias Holder,[1] Stephen D. Wilson,[3] Harald O. Jeschke,[4] and Alon Ron[1]

[1] *Raymond and Beverly Sackler School of Physics and Astronomy, Tel-Aviv University, Tel Aviv, 69978, Israel*
[2] *Technische Hochschule Brandenburg, Magdeburger Straße 50, 14770 Brandenburg an der Havel, Germany*
[3] *Materials Department, University of California, Santa Barbara, California, 93106, USA*
[4] *Research Institute for Interdisciplinary Science, Okayama University, Okayama 700-8530, Japan*

S1 - DATA ANALYSIS USING ρ RATHER THAN WITH σ

Throughout the manuscript, we chose not to work with conductivity but rather with resistivity for the following reason: Calculations of ρ_{xx} and ρ_{xy} from resistance data incorporate division by multiplicative factors, c_{xx} and c_{xy} respectively, originating from geometry. In contrast to experiments under ambient conditions in which the sample geometry could be well defined and the positions of the leads determined to great accuracy, experiments in a DAC result in inevitable uncertainties in c_{xx} and c_{xy}. These result in a linear multiplicative factor for ρ_{xx} and ρ_{xy}. In contrast, the extraction of the conductivity values involves the inversion of the resistivity matrix, which results in the following expression for the transverse conductivity: $\sigma_{xy} = -\frac{\rho_{xy}}{\rho_{xx}^2+\rho_{xy}^2}$, when expressed as a function of the measured quantities as well as c_{xx} and c_{xy} the following form is obtained: $\sigma_{xy} = -\frac{\frac{R_{xy}}{c_{xy}}}{(\frac{R_{xx}}{c_{xx}})^2+(\frac{R_{xy}}{c_{xy}})^2}$. This nonlinear relation between σ_{xy} and the inevitable error in c_{xx} and c_{xy} will result in resistivity dependent errors in the estimation of any conductivity quantities from our data.

Throughout the manuscript the data in both samples was factored by a geometric factor of order unity which was extracted by comparing the resistivity and Hall coefficients at pressure points common to both samples (7.5 GPa).

S2 - THE MIT - R(T) AT DIFFERENT PRESSURES

The longitudinal resistance as a function of temperature, normalized at 9.5 K, measured at different pressures in the first cell. The change in the behavior of the graph from decreasing to increasing as a function of the temperature in the low-temperature regime by application of pressure indicates a metal-insulator transition driven by the application of pressure on the $CrGeTe_3$.

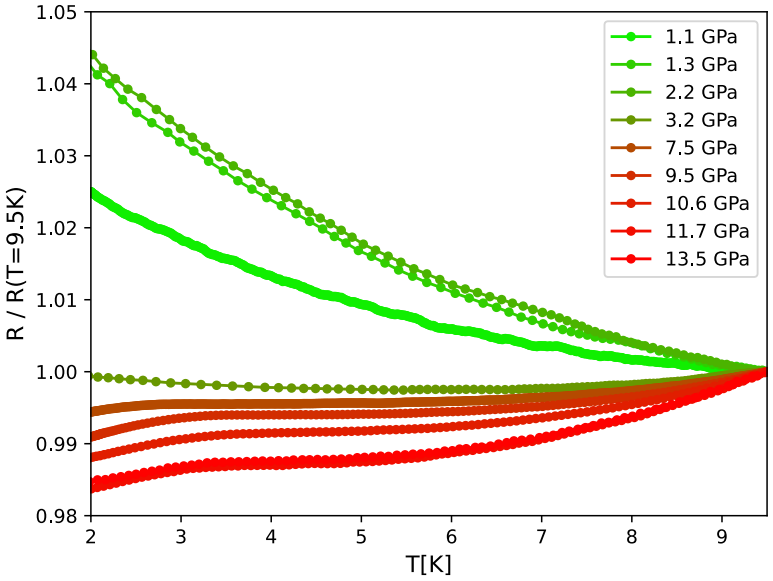

FIG. S1: The longitudinal resistance as a function of temperature, normalized at 9.5 K, measured at different pressures in the first cell. The change in the behavior of the graph from decreasing to increasing as a function of the temperature by application of pressure indicates a MIT driven by the application of pressure on the $CrGeTe_3$.

S3 - ρ_{xx} AT DIFFERENT PRESSURES AND TEMPERATURES

In Figure S3, we present the longitudinal resistivity as a function of temperature in the metallic state, measured on both samples. As can be seen, they show very similar behavior as all of them are monotonic - increasing with the temperature and showing similar values. As such, going back to our measurements of the AHE as a function of the temperature (see Figures 2 and S9), the observed behaviors cannot be explained just by the scaling of ρ_{AHE} with the ρ_{xx}. First, the scaling of ρ_{xx} cannot explain the change in the behavior of the AHE between the intermediate pressure regime ($5.6 < P < 13$ GPa) and the high-pressure regime (13 Gpa $< P$). Second, it cannot explain why at 13.5 GPa, the AHE is stronger than at higher pressures in the first sample and thus probably not also in the second cell. Finally, going back to the low-temperature behavior of the AHE as shown in Figure 4, the values of ρ_{xx} at low temperatures (shown in log-scale in Figure S4) cannot explain the dome-like behavior of the AHE.

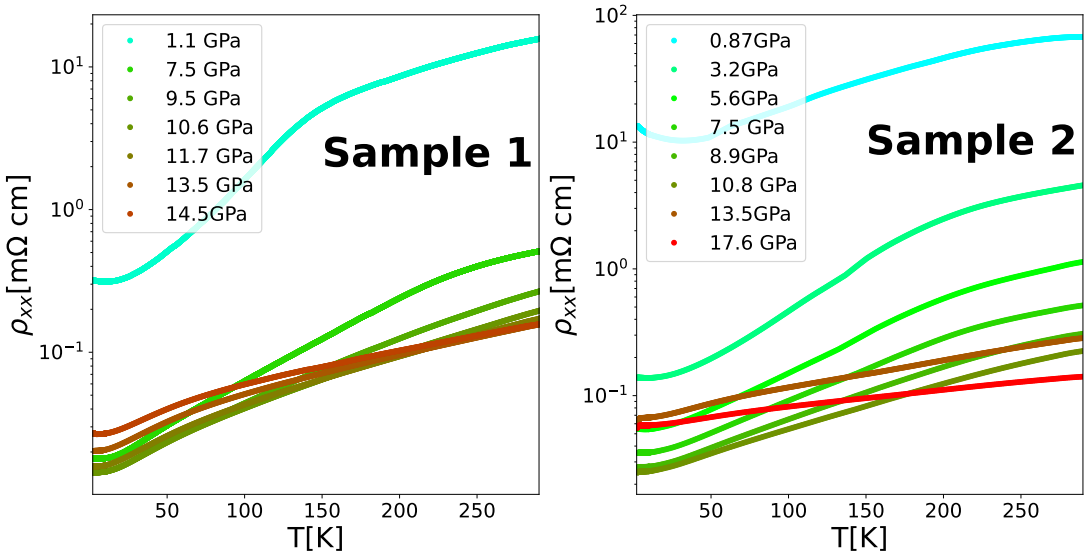

FIG. S2: The longitudinal resistivity as a function of temperature at different pressures presented in log-scale, on the left in the first sample and on the right in the second sample.

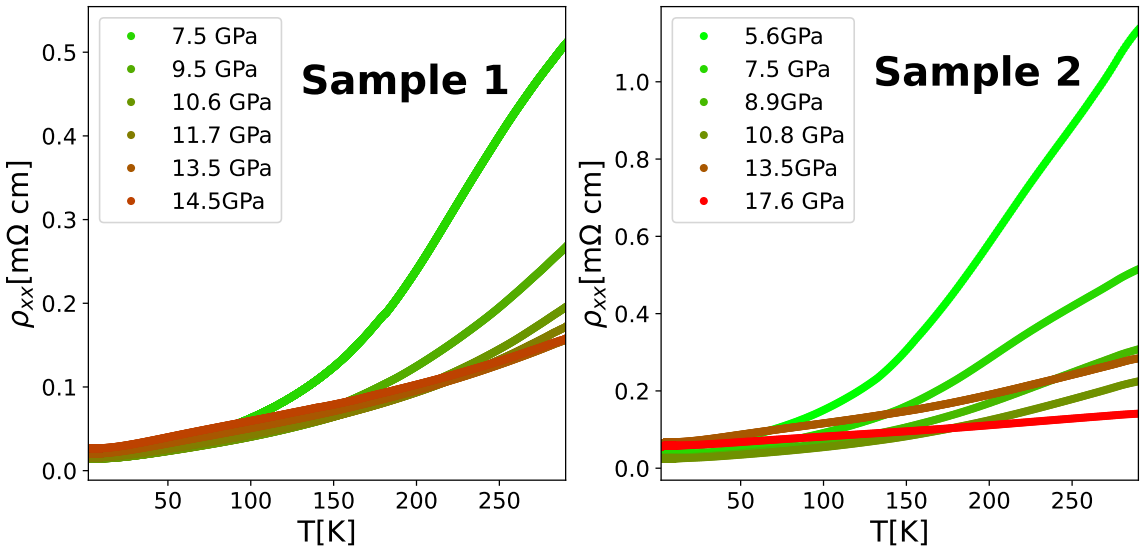

FIG. S3: The longitudinal resistivity as a function of temperature at different pressures in the metallic state, on the left in the first sample and on the right in the second sample.

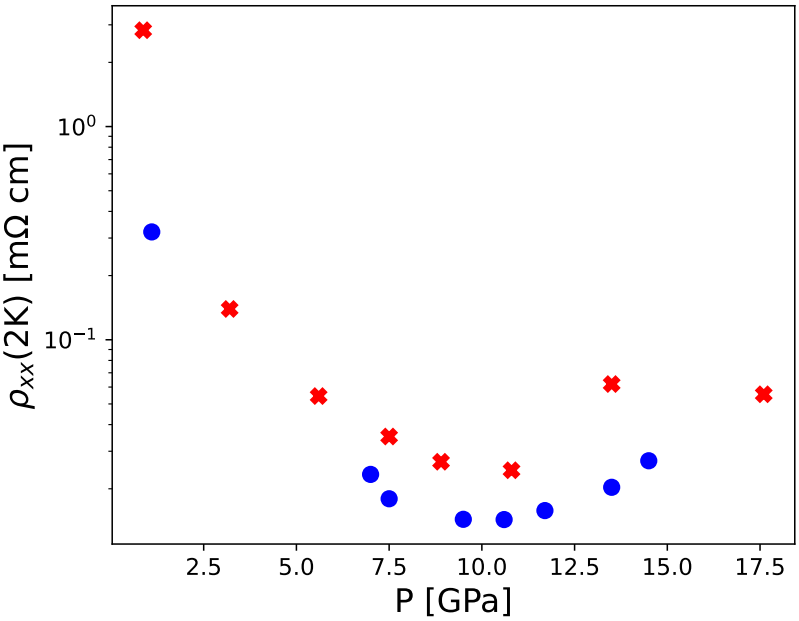

FIG. S4: The longitudinal resistivity at low temperature (2 K) as a function of the pressure in log-scale. The Blue and the red points are from the first and second cells, respectively. Their resistivity values are scaled by a single geometric factor of order unity which was used throughout the manuscript for each longitudinal measurement.

S4 - THE HALL SLOPES MEASURED AT DIFFERENT PRESSURES AND TEMPERATURES

Here, we present the Hall slopes as a function of temperature, measured at different pressures. In most measurements, the Hall slope is positive, meaning that although there is a mix of electrons and holes in all pressures, in most of the pressures, we can treat the transport as of hole-like charge carriers. However, at 3.2 GPa and 14.5 GPa, there is a change in the sign of the Hall slope, indicating that at these pressures, both holes and electrons contribute to transport where their contributions are temperature dependent, which can also be seen in Figure 1 (b) in the text. At these pressures, we cannot treat the transport as dominated by a single charge carrier. The fact that the Hall slope changes sign as a function of the temperature at those pressures but not before might indicate changes in the band structure of the $CrGeTe_3$, which may result in a change in the integrated Berry curvature.

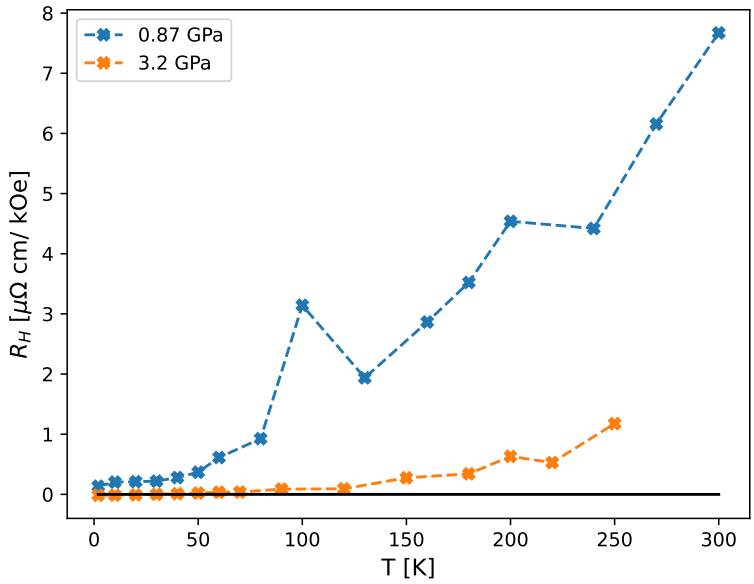

FIG. S5: The Hall slopes as a function of temperature, measured at 0.87 GPa and at 3.2 GPa.

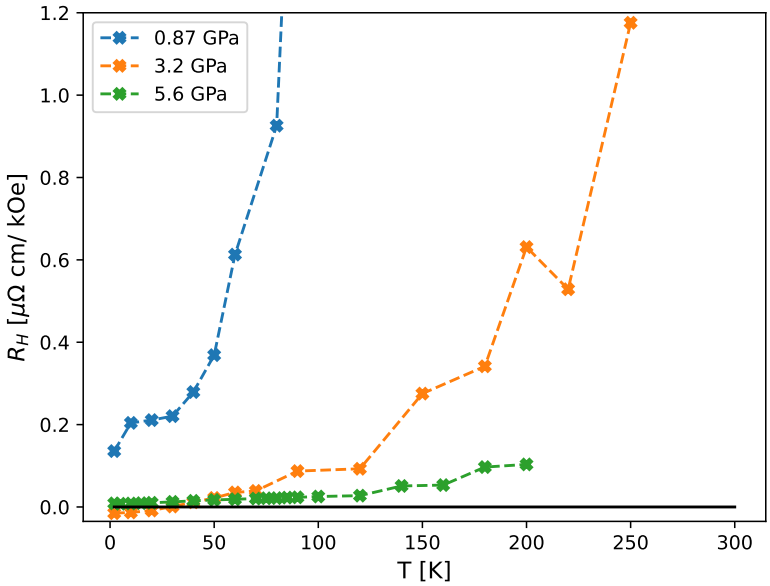

FIG. S6: The Hall slopes as a function of temperature, measured at 0.87 GPa, 3.2 GPa, and 5.6 GPa.

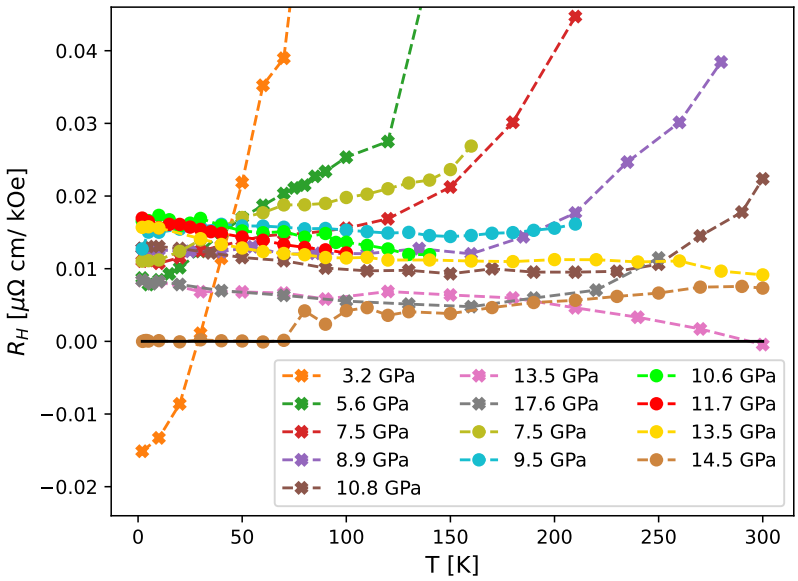

FIG. S7: The Hall slopes as a function of temperature, measured at different pressures. The dots represent data from the first cell, and the Xs denote measurements from the second cell.

S5 - THE EXTRACTION OF ρ_{AHE} FROM THE MEASUREMENTS

ρ_{AHE} in a specific temperature and pressure, is extracted from the measurements by measuring $R_{xy}(H)$ and antisymmetrize it. This results in graphs as shown in section S6. Then we do a linear fit to the high-field regime ($4\,\mathrm{kOe} < H$), and the intersection of the fit with the y-axis is the AHE resistance (R_{AHE}) (see Fig.S8). Finally, by multiplying R_{AHE} with the width of the sample, we get ρ_{AHE}.

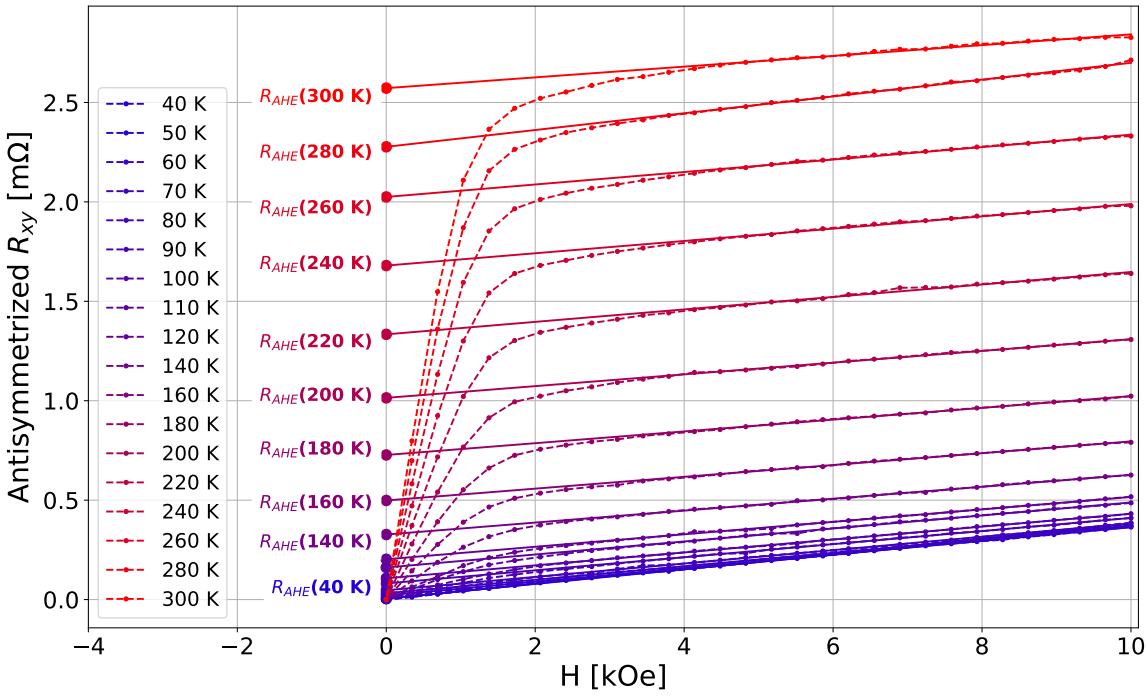

FIG. S8: Here we show an example of how we extracted the AHE resistance (R_{AHE}) for each pressure at different temperatures. The figure displays the antisymmetrization of the raw data of R_{xy} as a function of the applied field H, measured at several different temperatures for the first sample in the metallic state at a pressure of 13.5 GPa. The solid lines are the linear fit for the high-fields regime ($4\,\mathrm{kOe} < H$) at each temperature, and the big dots represent the intersection of each fit with the y-axis. The intersection of each fit is R_{AHE} measured at each temperature.

S6 - THE AHE MEASURED IN THE FIRST CELL

Here we present our measurements of ρ_{AHE} as a function of temperature for the various pressures measured in the first sample. As was also observed in the second sample (in the main text), At pressures below 13 GPa, $\rho_{AHE} \neq 0$ at low temperatures and decays smoothly as the temperature increases. In contrast, for P > 13 GPa, at low temperatures $\rho_{AHE} = 0$, and increases as the temperature increases.

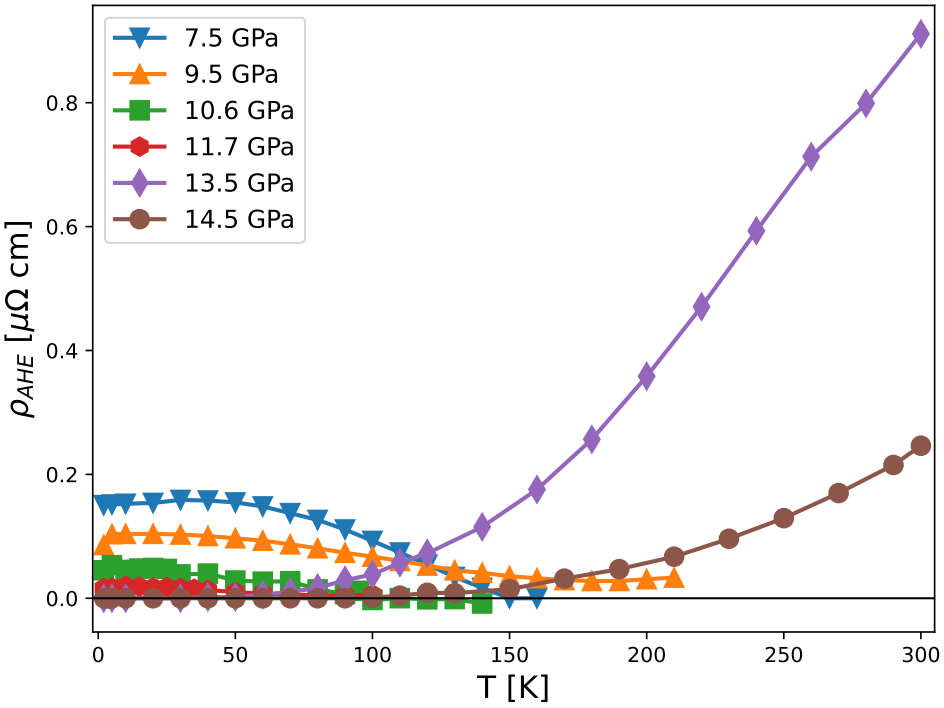

FIG. S9: ρ_{AHE} as a function of temperature for the various pressures measured for sample 1.

S7 - RAW DATA MEASUREMENTS OF R_{xy} AND THE RESULTED ANTI-SYMMETRIC PLOTS FOR ALL PRESSURES AND CELLS

Here we present measurements of R_{xy} as a function of the applied field H at various pressures and temperatures, both in their raw form and after undergoing antisymmetrization. When there is significant mixing of R_{xx} and R_{xy} in the measurements, it is reflected in the raw data, which appears neither symmetric nor antisymmetric. This effect has been observed multiple times, particularly in the low-pressure regime before the metal-insulator transition.

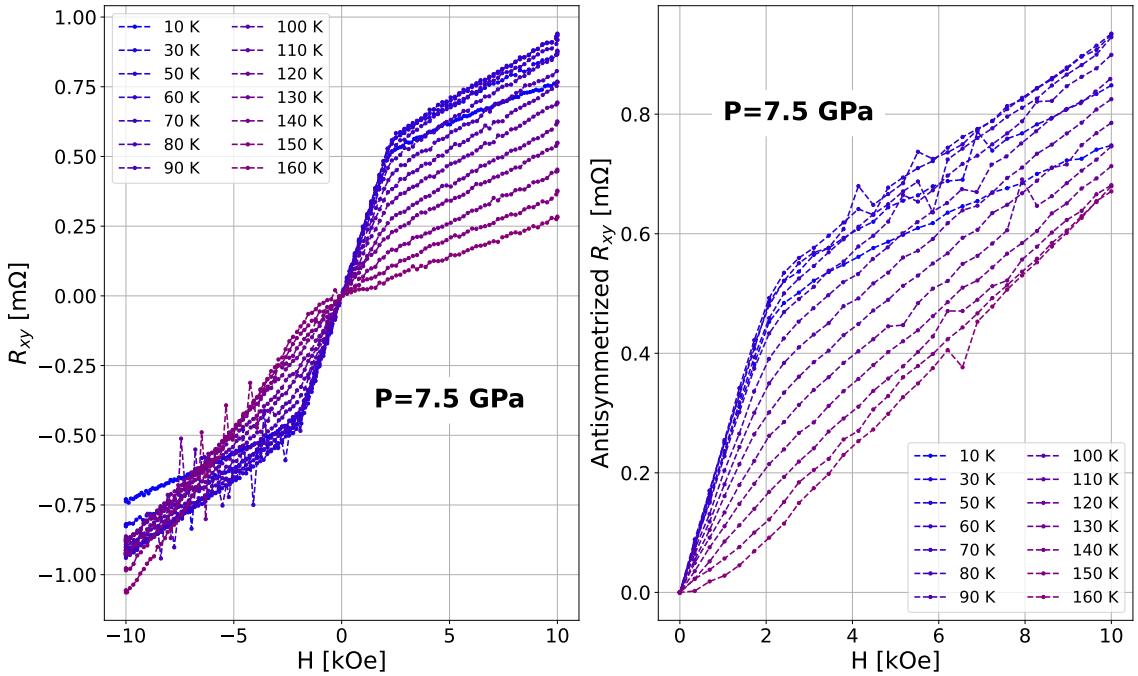

FIG. S10: The left panel displays the raw data of R_{xy} as a function of the applied field H for the first sample in the metallic state at a pressure of 7.5 GPa. The right panel shows the same data after antisymmetrization.

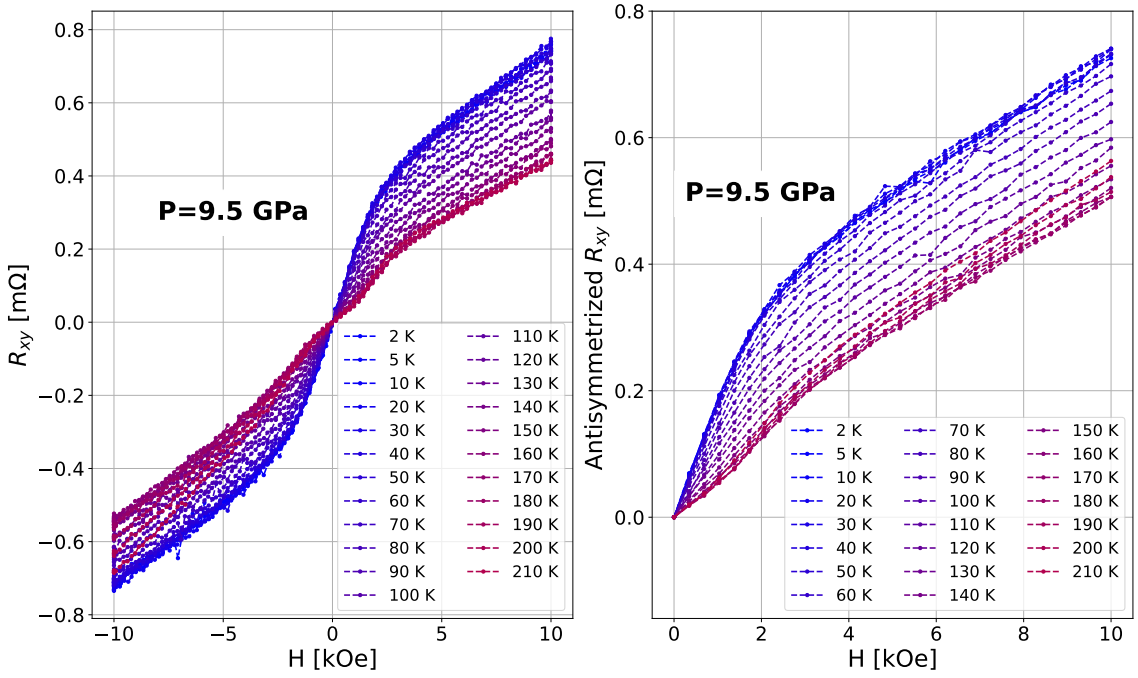

FIG. S11: The left panel displays the raw data of R_{xy} as a function of the applied field H for the first sample in the metallic state at a pressure of 9.5 GPa. The right panel shows the same data after antisymmetrization.

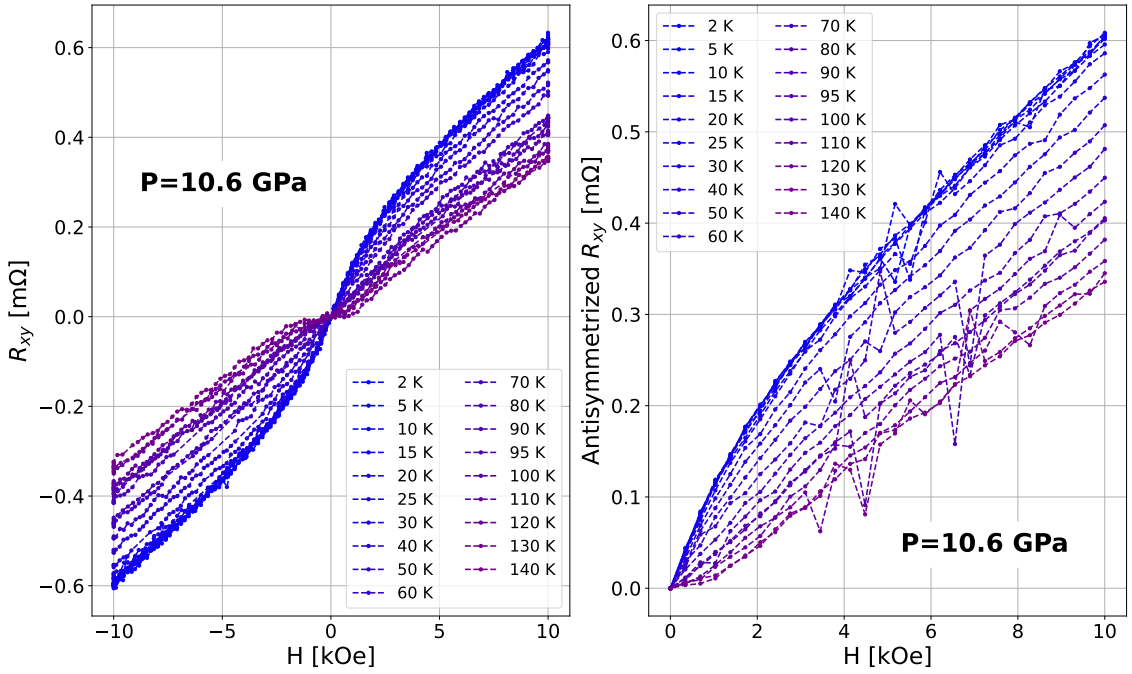

FIG. S12: The left panel displays the raw data of R_{xy} as a function of the applied field H for the first sample in the metallic state at a pressure of 10.6 GPa. The right panel shows the same data after antisymmetrization.

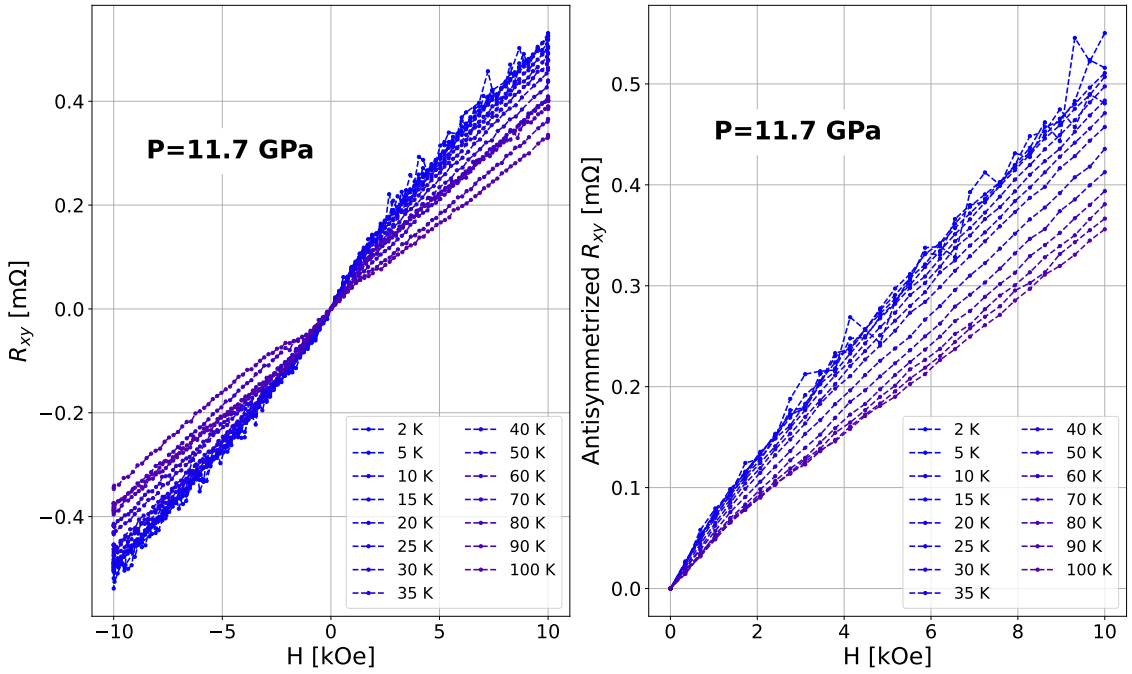

FIG. S13: The left panel displays the raw data of R_{xy} as a function of the applied field H for the first sample in the metallic state at a pressure of 11.7 GPa. The right panel shows the same data after antisymmetrization.

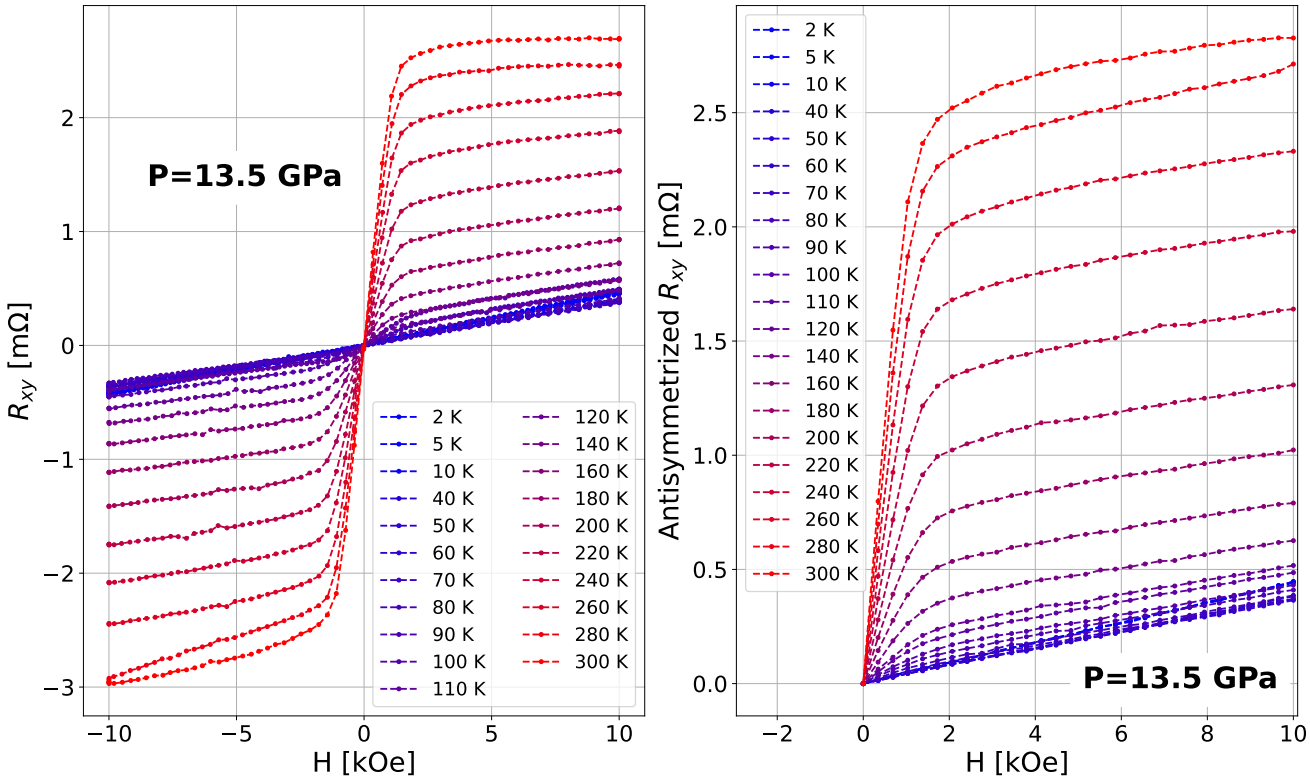

FIG. S14: The left panel displays the raw data of R_{xy} as a function of the applied field H for the first sample in the metallic state at a pressure of 13.5 GPa. The right panel shows the same data after antisymmetrization.

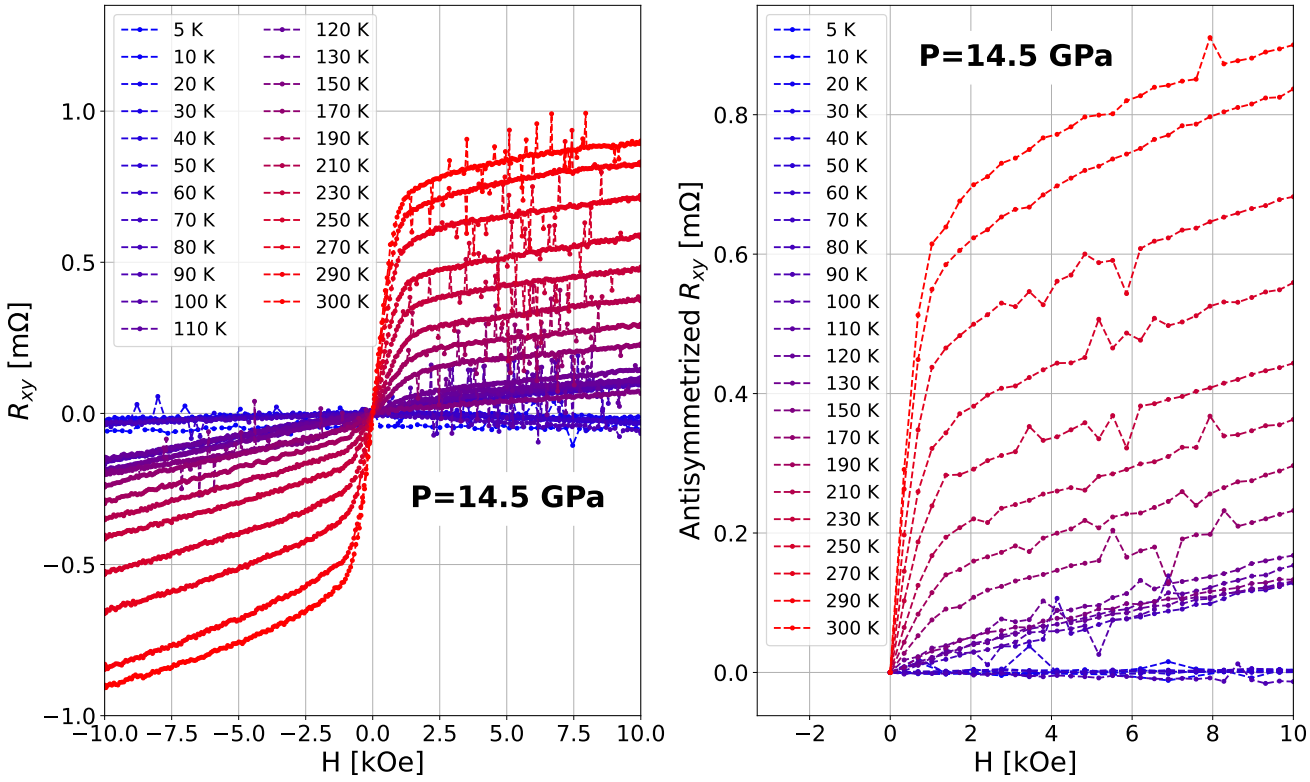

FIG. S15: The left panel displays the raw data of R_{xy} as a function of the applied field H for the first sample in the metallic state at a pressure of 14.5 GPa. The right panel shows the same data after antisymmetrization.

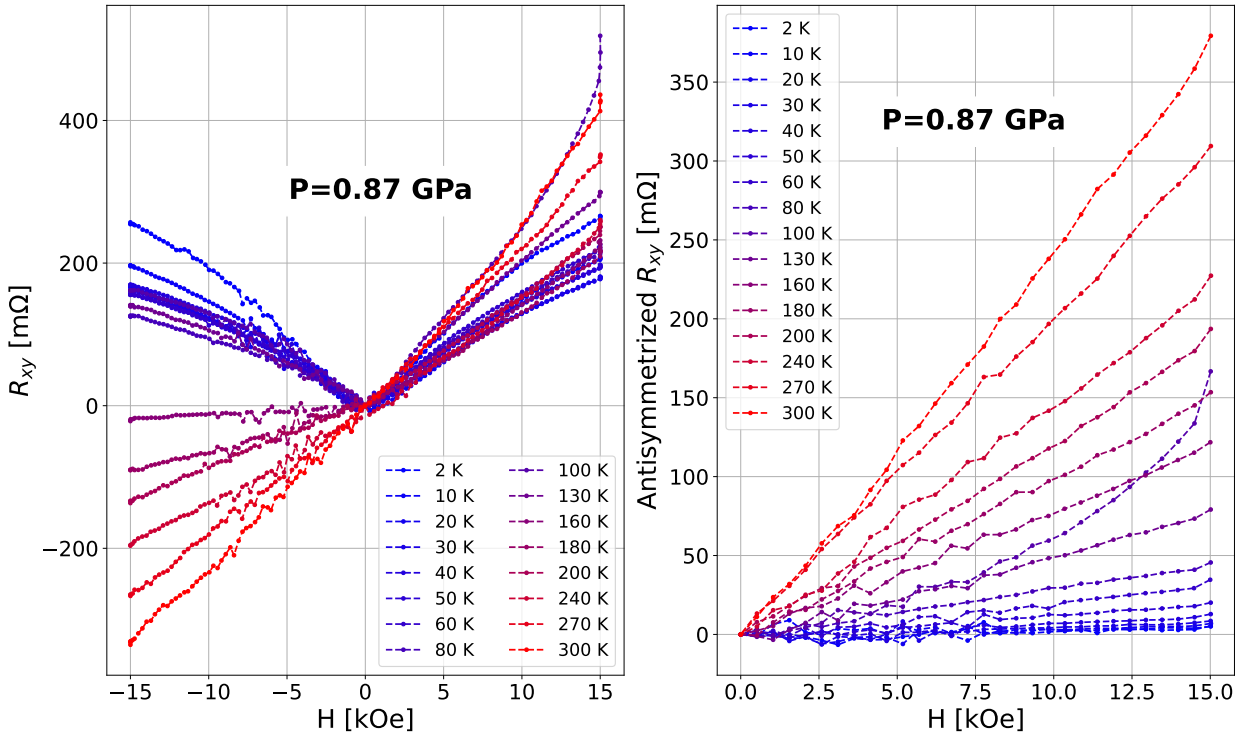

FIG. S16: The left panel displays raw data of R_{xy} as a function of the applied field H for the second sample in the insulating state at a pressure of 0.87 GPa. The right panel presents the same data after antisymmetrization. The presence of significant intermixing between R_{xx} and R_{xy} can be easily identified by the absence of symmetry or antisymmetry in the raw data.

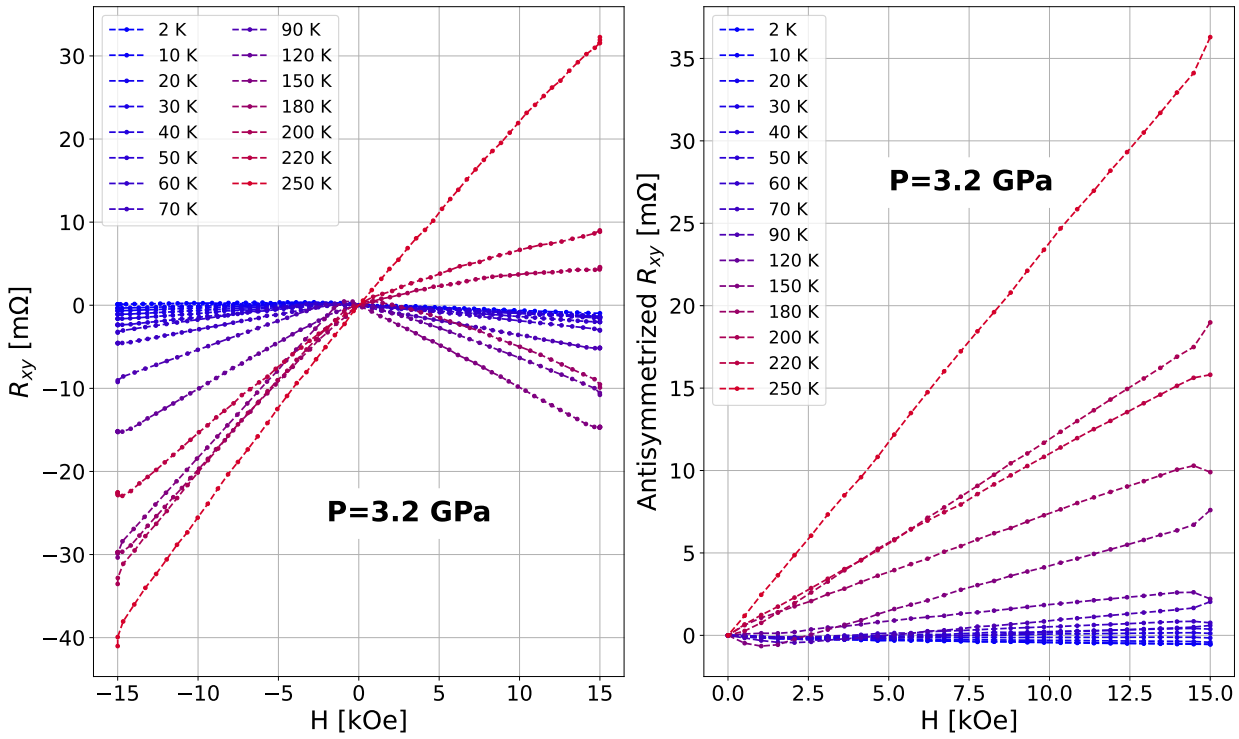

FIG. S17: The left panel displays raw data of R_{xy} as a function of the applied field H for the second sample in the insulating state at a pressure of 3.2 GPa. The right panel presents the same data after antisymmetrization. The presence of significant intermixing between R_{xx} and R_{xy} can be easily identified by the absence of symmetry or antisymmetry in the raw data.

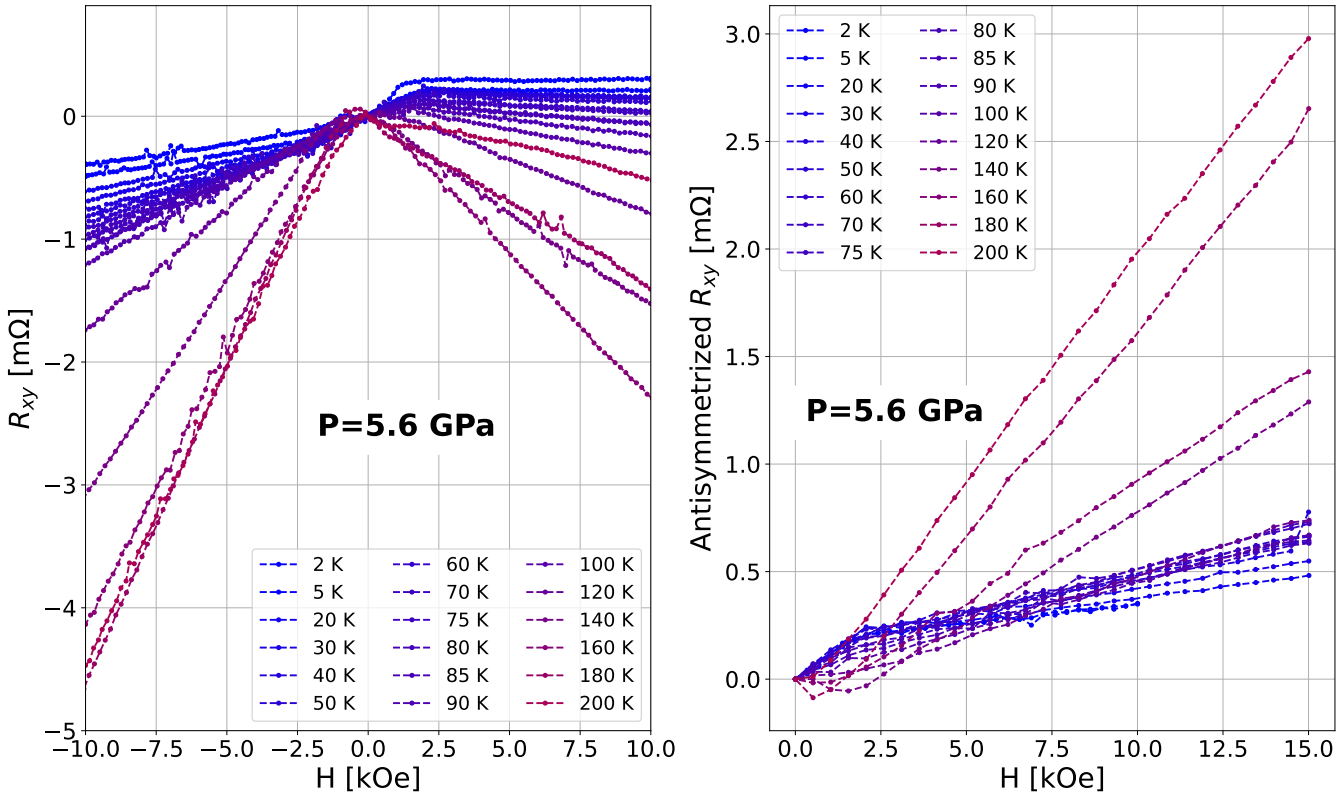

FIG. S18: The left panel displays the raw data of R_{xy} as a function of the applied field H for the second sample in the metallic state at a pressure of 5.6 GPa. The right panel shows the same data after antisymmetrization.

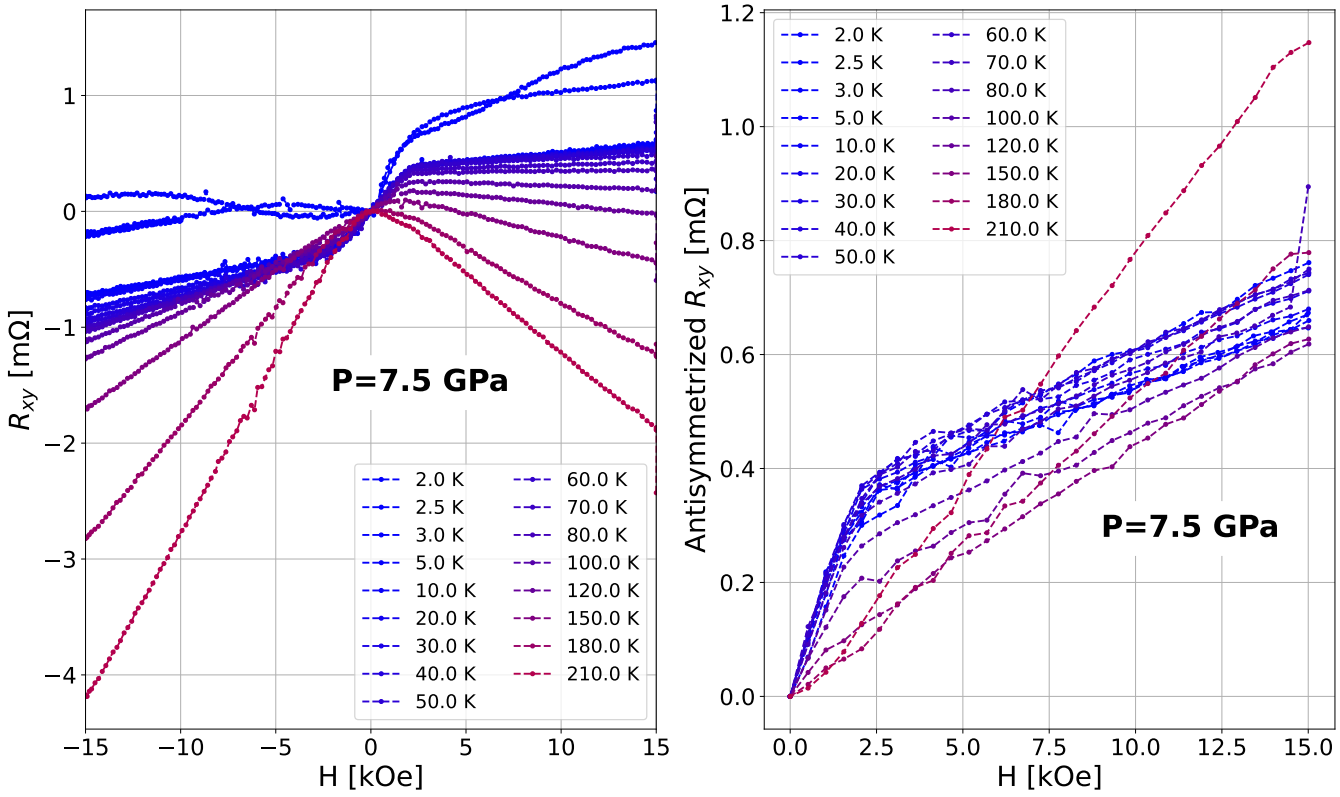

FIG. S19: The left panel displays the raw data of R_{xy} as a function of the applied field H for the second sample in the metallic state at a pressure of 7.5 GPa. The right panel shows the same data after antisymmetrization.

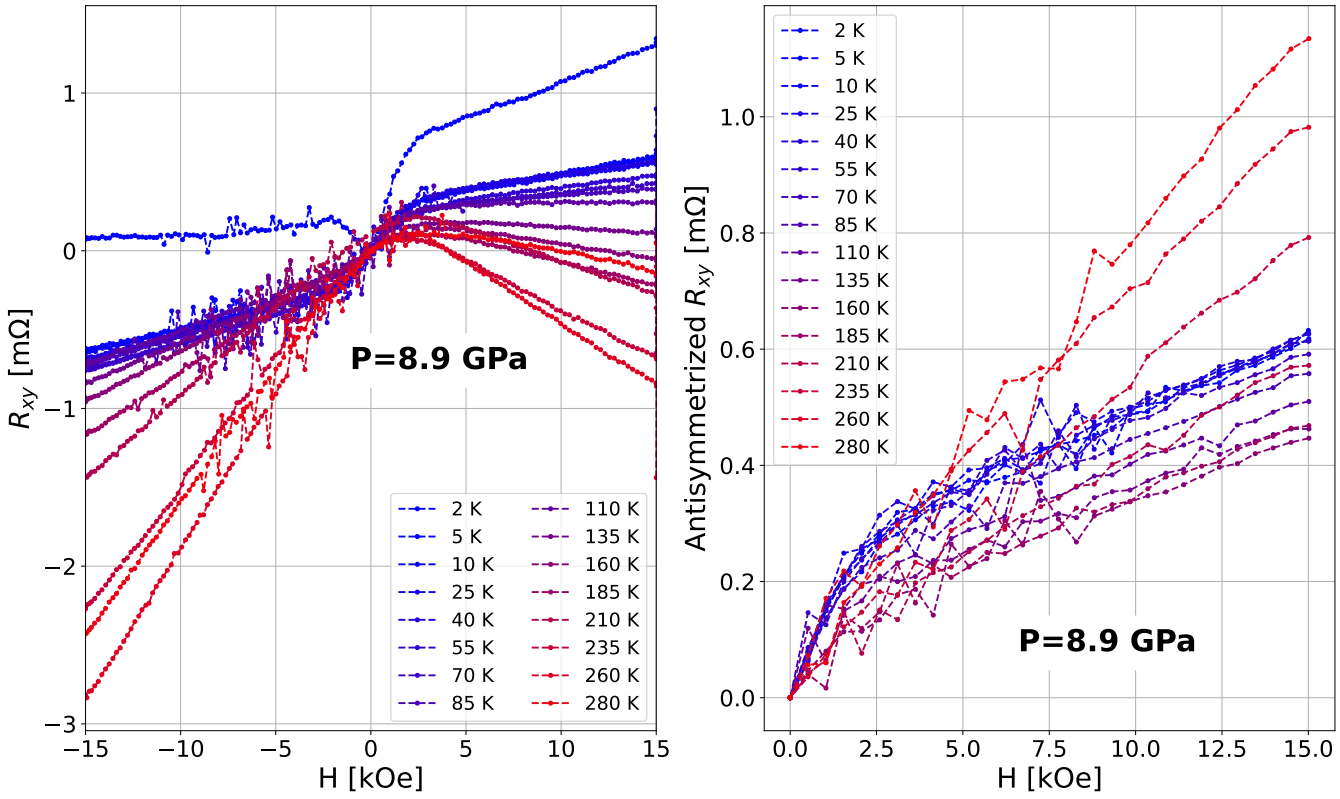

FIG. S20: The left panel displays the raw data of R_{xy} as a function of the applied field H for the second sample in the metallic state at a pressure of 8.9 GPa. The right panel shows the same data after antisymmetrization.

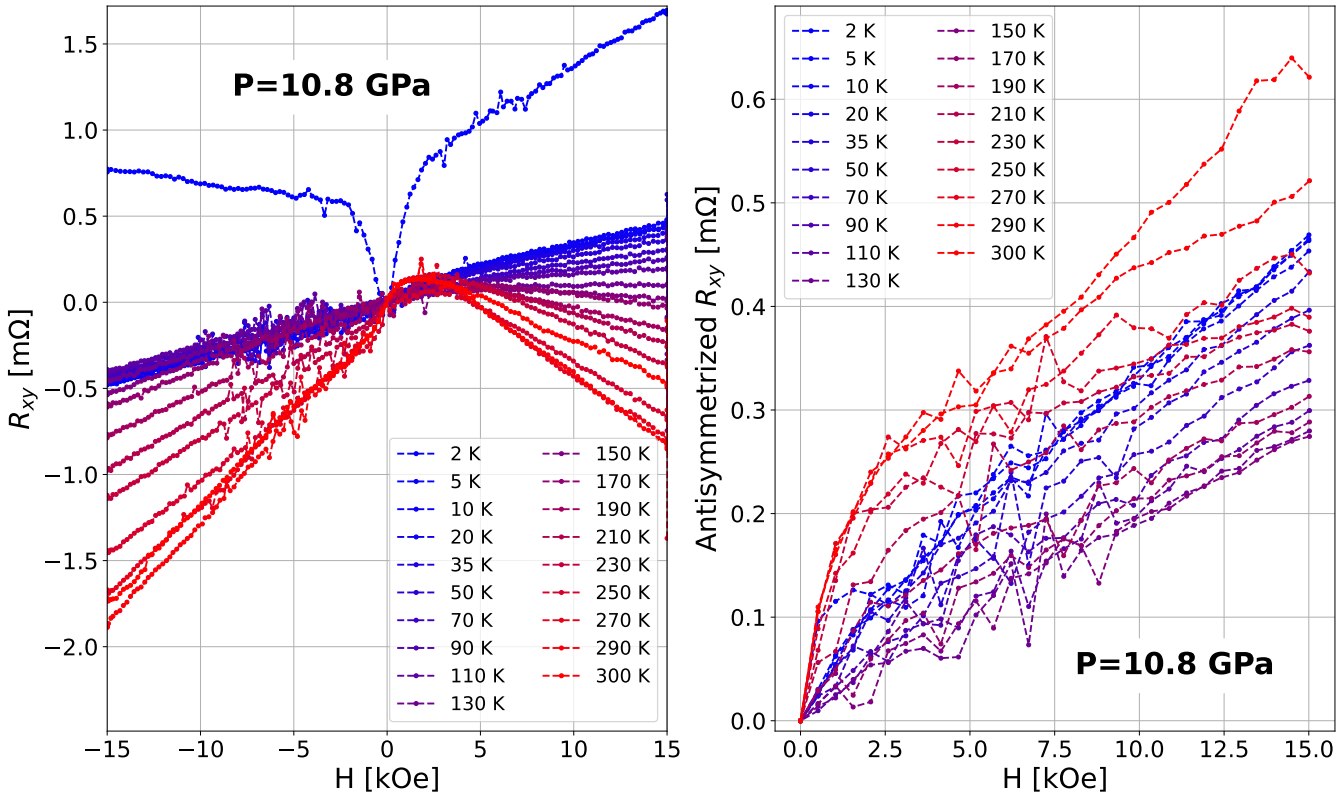

FIG. S21: The left panel displays the raw data of R_{xy} as a function of the applied field H for the second sample in the metallic state at a pressure of 10.8 GPa. The right panel shows the same data after antisymmetrization.

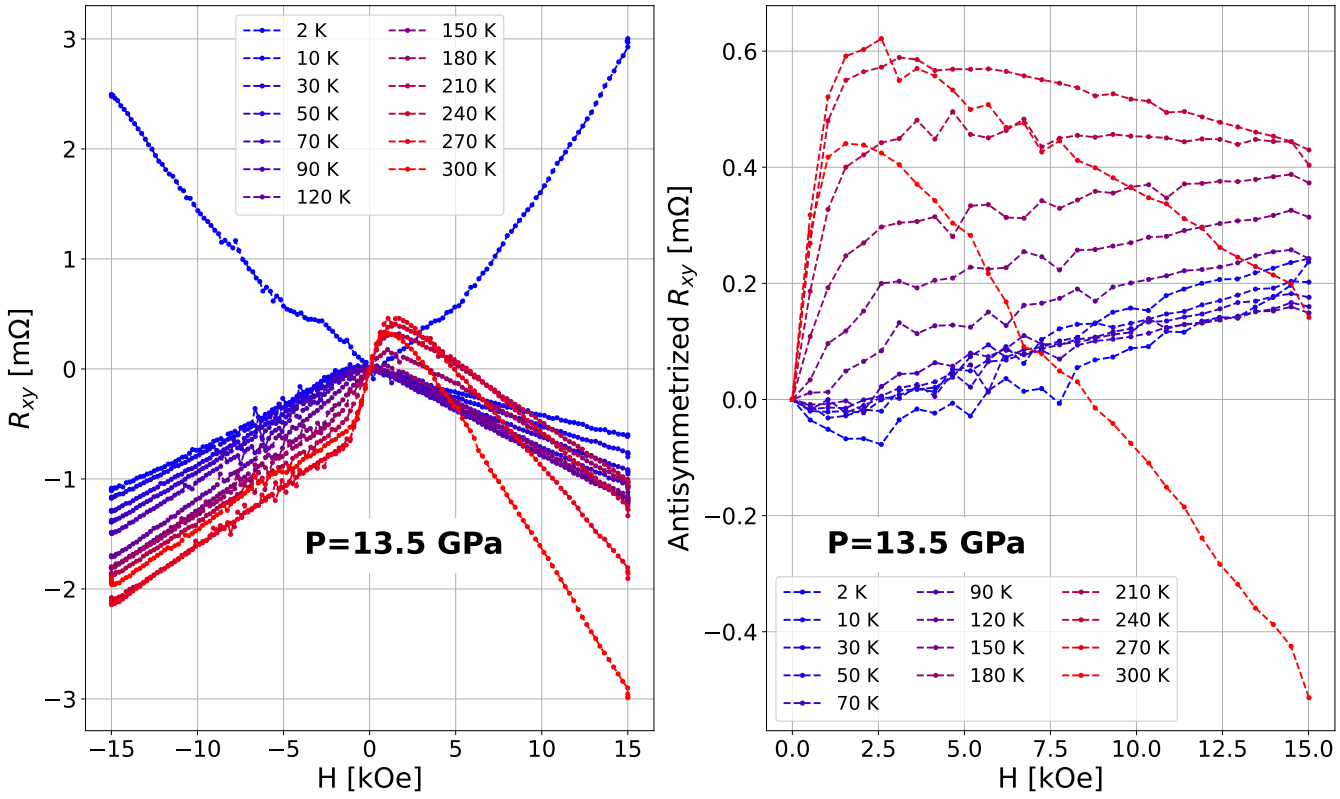

FIG. S22: The left panel displays the raw data of R_{xy} as a function of the applied field H for the second sample in the metallic state at a pressure of 13.5 GPa. The right panel shows the same data after antisymmetrization.

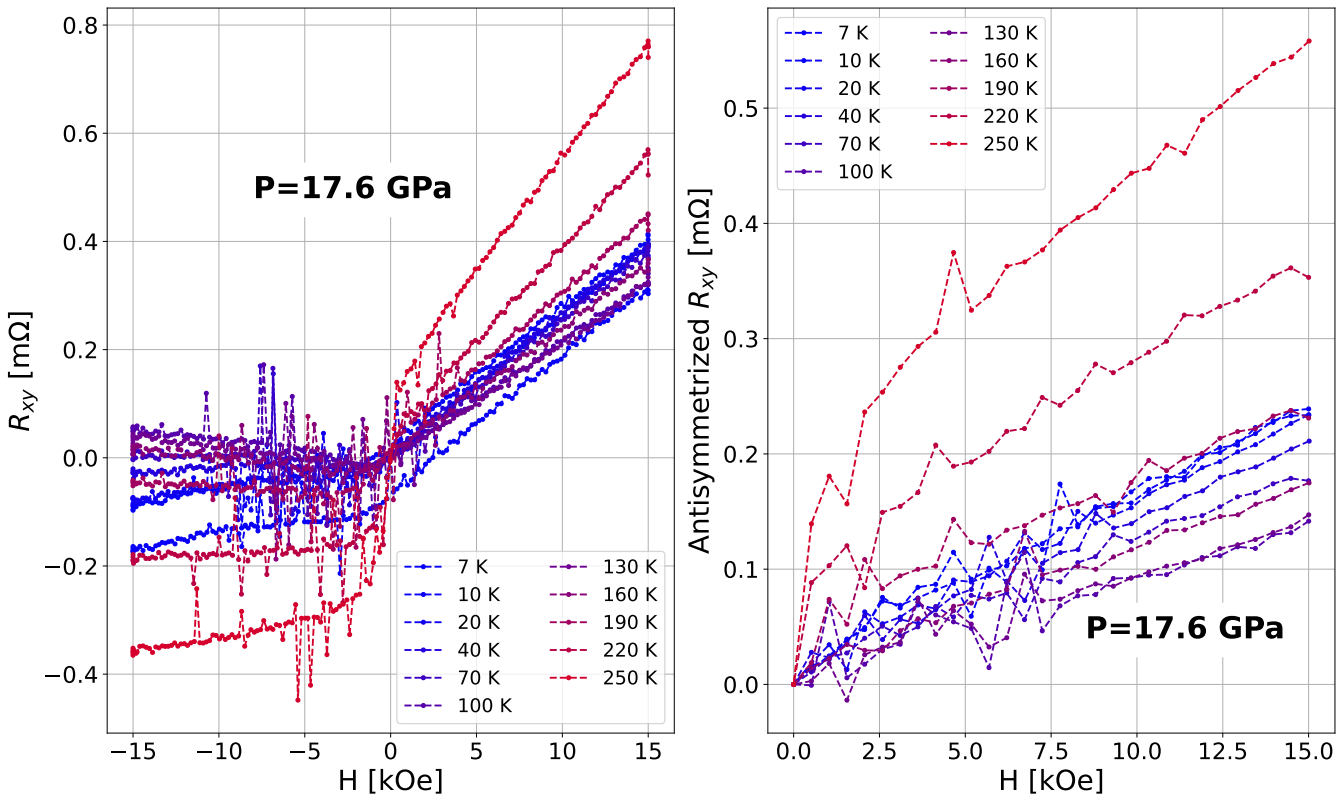

FIG. S23: The left panel displays the raw data of R_{xy} as a function of the applied field H for the second sample in the metallic state at a pressure of 17.6 GPa. The right panel shows the same data after antisymmetrization.

S8 - EFFECT OF MAGNETIC QUANTIZATION AXIS ROTATION ON BERRY CURVATURE

We have performed additional DFT calculations, where we rotated the quantization axis (equivalent to the direction of magnetic field) from the k_z-direction towards the k_x-direction. For these additional calculations we evaluated the Berry curvature for $5 \cdot 10^5$ k-points for each pressure value and rotation angle in each of the ten independent Monte Carlo calculations.

The rotation of the quantization axis leads to a small but systematic effect on the anomalous Hall conductivity, which is shown in Fig. S24.

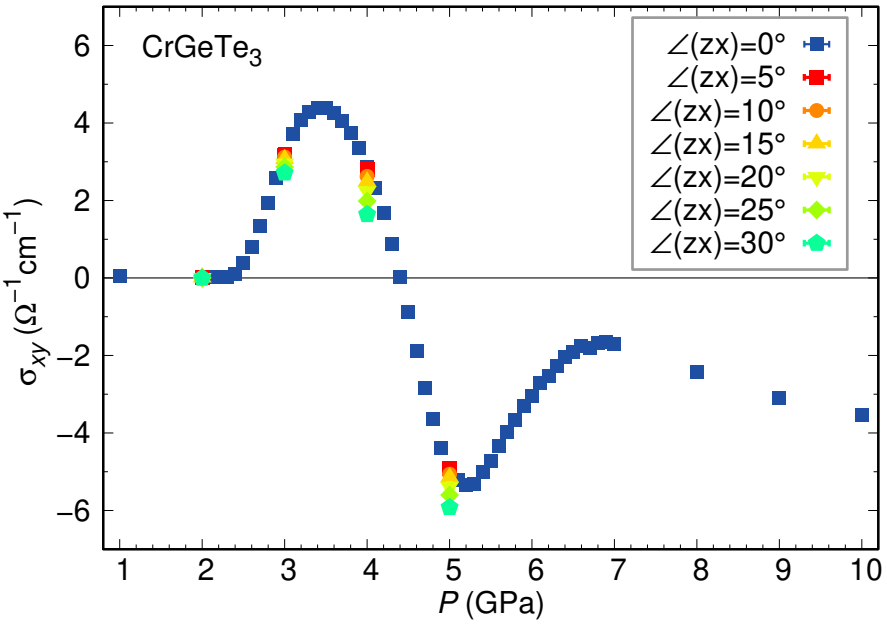

FIG. S24: Sensitivity of anomalous Hall conductivity on the direction of the quantization axis. The angle denotes the rotation from the k_x-direction towards the k_z-direction.

S9 - VARIATION OF THE SPIN-ORBIT COUPLING STRENGTH IN THE BAND STRUCTURE

In Fig. S25, we compare band structures without and with spin-orbit coupling for two values of pressure. High symmetry points of the rhombohedral space group are $L = (1/2, 0, 0)$, $A = (\nu/2, \nu/2, -\nu)$, $P = (\eta, \nu, \nu)$, $Z = (1/2, 1/2, 1/2)$, $X = (\nu, 0, -\nu)$ where $\eta = (1+4\cos\alpha)/(2+4\cos\alpha)$, $\nu = 3/4-\eta/2$, and α is the rhombohedral angle [S1]. At these pressures, bands near Γ and X points cross the Fermi level, forming hole and electron pockets, respectively. The corresponding Fermi surfaces are displayed in Figs. 5 (c) and (d) of the main text. By comparing scalar relativistic and fully relativistic bands, we notice that they barely differ for the electron pocket at the X point. This is because the character is dominantly Cr $3d$ (see band weights in Figs. 6 (c) and (d) of the main text), and consequently the Berry curvature near the X point pocket is small (also shown in Figs. 6 (c) and (d) of the main text). On the other hand, spin-orbit coupling has a very strong effect near the Γ point, seen as large deviation between GGA (black) and GGA+SO (blue) bands near Γ in Fig. S25. This correponds to dominant Te $5p$ character for these bands (see band weights in Figs. 6 (c) and (d) of the main text), and to very high Berry curvature amplitudes where these strongly spin-orbit coupled bands cross the Fermi level (also shown in Figs. 6 (c) and (d) of the main text).

[S1] W. Setyawan and S. Curtarolo, High-throughput electronic band structure calculations: Challenges and tools, Comput. Mater. Sci. **49**, 299 (2010).

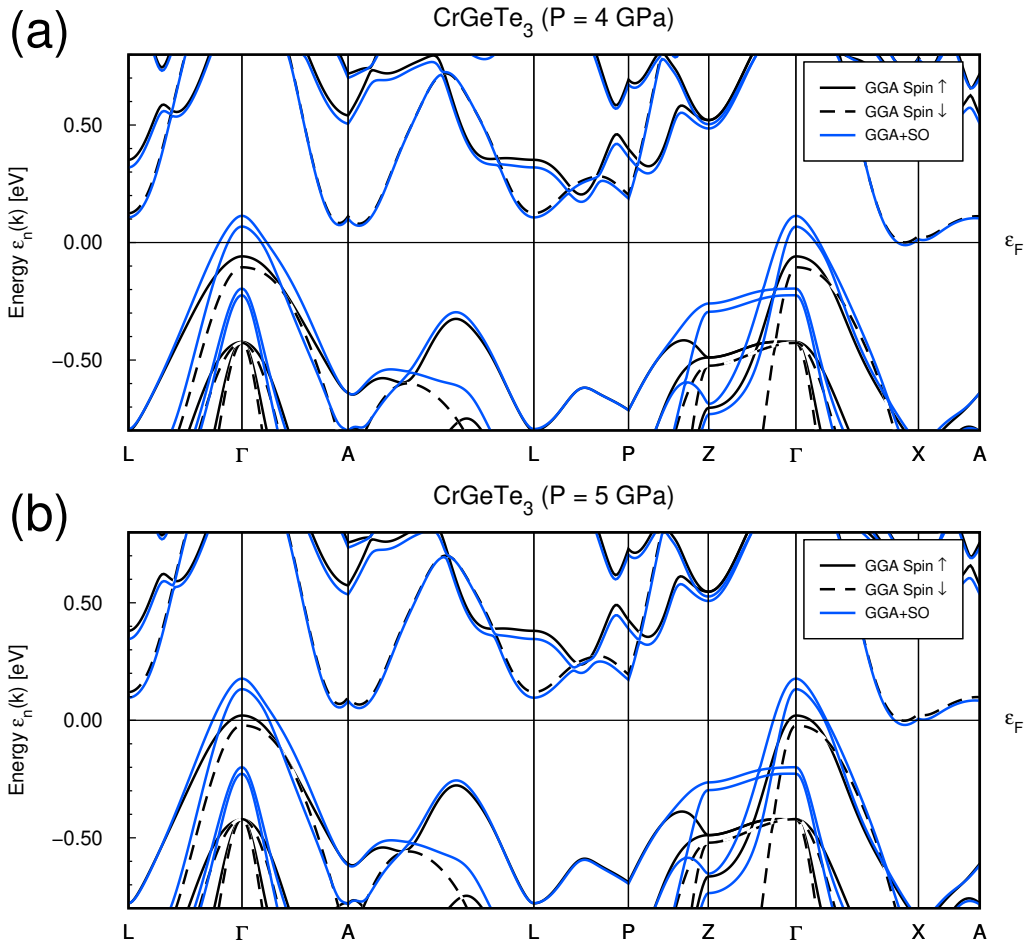

FIG. S25: Comparison between scalar relativistic (GGA) and fully relativistic (GGA+SO) band structures for $CrGeTe_3$ at (a) $P = 4\,\mathrm{GPa}$ and (b) $P = 5\,\mathrm{GPa}$. For the definition of the high symmetry points, see the text.